

Rotation Measures of Compact Sources in the Canadian Galactic Plane Survey

J.C. Brown, A.R. Taylor and B.J. Jackel

*Department of Physics and Astronomy, University of Calgary, Calgary, Alberta, Canada
T2N 1N4*

ABSTRACT

The Canadian Galactic Plane Survey is providing new rotation measures (RMs) for compact extragalactic sources in the Galactic plane at a solid-angle density of roughly 1 source per square degree. To date, we have derived reliable RM values for 380 sources along lines of sight through the disk of the Galaxy in the first and second quadrants. The purpose is to provide a data set useful for studies of the magneto-ionic component of the Galactic interstellar medium (ISM). We present the method used to obtain the measurements and the resulting RMs.

Subject headings: catalogs—ISM:magnetic fields—polarization—radio continuum:galaxies—
techniques:polarimetric

1. Introduction

Studies of the Galactic magnetic field may be pursued by observing the effect of the field on polarized radiation passing through the regions of the interstellar medium (ISM) which it occupies. The signature of the magnetic field can be observed as a rotation of the polarization angle of the radiation from polarized sources, both Galactic (usually pulsars) and extragalactic (galaxies and quasars). The amount of rotation is characterized by the rotation measure (RM) which is defined by

$$\text{RM} = 0.812 \int n_e \mathbf{B} \cdot d\mathbf{l} \text{ [rad]}, \quad (1)$$

where n_e [cm^{-3}] is the electron density, $d\mathbf{l}$ [pc] is an increment of the path length through the magnetized plasma, and \mathbf{B} [μG] is the magnetic field. The sign dependence of the RM resulting from the dot-product between \mathbf{B} and the path (defined from the source to the

receiver) makes RMs particularly useful in studying the structure of the Galactic magnetic field.

Since observation of these sources provides information on the line-of-sight component of the field, the more sources available for observation, the more information that can be extracted about the field. Many catalogues of RMs for extragalactic sources exist (ex. Simard-Normandin et al. 1981; Broten et al. 1988; Clegg et al. 1992; Oren & Wolfe 1995). However, the majority of the published RM sources are located at high Galactic latitudes, and thus provide little information for studies focusing on the magnetic field within the disk.

The location and resolution of the Canadian Galactic Plane Survey (CGPS) provide a new opportunity to study RM sources with a dense set of sight-lines through the thick disk, where the Galactic magnetic field is generally believed to be concentrated (Simard-Normandin & Kronberg 1980; Han & Qiao 1994). As part of a study of the magnetic field in the disk of the Galaxy (Brown 2002), we have derived the RM of 380 compact sources within the CGPS in the longitude intervals $115^\circ \leq l \leq 146^\circ$ and $82^\circ \leq l \leq 96^\circ$ ($-3.6^\circ < b < 5.6^\circ$). These sources were selected from a larger sample of polarized compact sources to satisfy the following criteria: a) the source has a well-defined polarized component; b) there are enough pixels on the source with suitable signal-to-noise to perform statistical analysis; c) the source is Faraday-thin, meaning it does not exhibit significant internal Faraday rotation; d) the RM is uniform over the area of the polarized component. Such sources are suitable probes of the magneto-ionic properties of the ISM.

A significant fraction ($\sim 80\%$) of compact sources observed in Stokes I at decimeter wavelengths are of extragalactic origin (ie. galaxies and quasars; Taylor et al. 1986; Butenhoff 1997). Of the Galactic compact sources, most are compact H II regions (Taylor et al. 1986). Only a small fraction are non-thermal sources (and therefore possibly polarized) such as compact supernova remnants and pulsars. Consequently, we expect very few of the compact polarized sources to be Galactic objects, and the vast majority to be extragalactic. In what follows, we present the RMs for the selected compact sources, and the method used to derive these values.

2. The Data

The CGPS is an international collaboration to map a 73° longitudinal section of the Galactic plane (Taylor et al. 2002). The goal of the CGPS is to develop a broader understanding of the states and processes of the ISM by observing multiple wavelength emissions from and through the ISM. As part of this project, observations of a 35 MHz band centered

on 1420 MHz are carried out using the Synthesis Telescope (ST) at the Dominion Radio Astrophysical Observatory (DRAO; Landecker et al. 2000). At this frequency, the ST has a resolution of $1'$ and a sensitivity of 0.28 mJy/beam or $0.071 \sin \delta$ K (noise-limited rms). In addition, it detects two orthogonal components of polarized radiation, providing the ability to measure the Stokes parameters.

The central 5 MHz of the 35 MHz band is used to synthesize images in the H I line only, while the remaining 30 MHz constitutes a continuum emission band. In order to reduce the effect of chromatic aberration, the continuum band is filtered into four 7.5 MHz sub-bands, labeled A–D. For the total intensity image (Stokes I), these sub-bands are recombined before the image is CLEANED (Taylor et al. 2002). For Stokes Q and U , the data are fully processed in the individual sub-bands. As of this writing, about one half of the CGPS data have been processed in polarization.

3. Calculating Rotation Measures

The process we use to calculate the RMs of compact sources involves three steps, as illustrated in the flowchart of figure 1. In step 1, we identify a source and verify that it is suitable for analysis. In step 2, we calculate the RM for all pixels on the source. In step 3, we use the calculations from the previous step to determine a single RM value toward the source.

3.1. Step 1: Source Identification

We identify compact polarized sources by examining corrected linear polarized intensity maps (L_c , see equation 12 in the appendix). We define a compact source to be an object which appears in the L_c map as a well-defined, bright, emitting region with a diameter no greater than $3'$.

Identifying compact sources in L_c maps is not always straightforward. Small-scale, structured emission from a foreground ‘Faraday screen’ can confuse low-intensity, polarized compact sources. A Faraday screen arises from electron density changes and/or magnetic field fluctuations across the sky which can then produce the appearance of structure in the large-scale, otherwise uniform polarized emission from within the Galaxy (see for example Gray et al. 1999). As a result of the spatial filtering by the ST (Taylor 1999), signal may appear in the L_c maps where there is no corresponding signal in the total intensity maps, an effect first observed by Wieringa et al. (1993) using the Westerbork Synthesis Radio

Telescope. An example of this effect is illustrated in figure 2 with a total intensity image (Stokes I) and an L_c image of a mosaic from the CGPS. The upper right quadrant of the L_c image contains emission which is not seen in the Stokes I image. To distinguish this effect from true polarized background sources, we examine the Stokes I images to verify the existence of a corresponding compact Stokes I counterpart.

Another issue is that of instrumental polarization resulting from ‘leakage’ of total intensity (Stokes I) into polarized signal (Stokes Q and U). For DRAO, this is caused by cross-talk between the left and right circularly polarized detection feeds (Smegal et al. 1997). The instrumental polarization is calibrated and corrected for in the data processing (Taylor et al. 2002). Residual instrument polarization errors are less than 1% of I over the CGPS images. We have taken a conservative approach and consider only those sources with fractional polarization ($m = L_c/I$) greater than 2%.

The last requirement for successful identification we place on the data is that the source have sufficient signal-to-noise to produce satisfactory statistics in the following steps of the RM calculations. As a result of the convolution of the sky emission with the synthesized beam of the ST, compact objects appear as a well-defined two-dimensional Gaussian in the images. Therefore, we fit each source with a two-dimensional Gaussian plus a constant offset, and use the parameters to identify the image pixels on the source, as well as an annulus around the source for foreground estimation (see step 2). With the fitted parameters (position, amplitude, major and minor full widths), we identify the pixels falling within the full width–half maximum (FWHM) region; that is, the ellipse defining the half peak amplitude of the Gaussian. The pixels within the ellipse are used to calculate the RM of the source. Typically, the number of pixels within the FWHM is between 5 and 15. Of the pixels in the FWHM region, we only use those pixels that have signal-to-noise ratios (S:N) of at least 5:1 (see appendix). If the number of such pixels within a given source is fewer than 5, we discard that source.

3.2. Step 2: RM Calculation per Pixel

An effect that must be considered prior to calculating RMs is the presence of polarized emission originating from within the Galaxy in the vicinity of the compact source. This may be considered ‘foreground emission’ since we are only interested in the polarized signal originating from the source itself. Thus, it is necessary to remove this foreground signal from the Stokes Q and U of the source. One method, implemented by Gaensler et al. (2001), is to filter the image so that only baselines corresponding to scale sizes on the order of compact sources are used, which effectively removes all large-scale contributions from

the image. Similarly, the ST effectively removes the largest scale foreground corresponding to structures of scale sizes larger than $40'$. We remove residual foreground emission from smaller-scale structures by measuring the emission in the region around the source and removing the median signal. Since Stokes parameters combine additively for independent waves (Thompson et al. 2001), we may consider the measured signal in Stokes Q (or U) as the sum of two signals, such that $Q_{\text{observed}} = Q_{\text{source}} + Q_{\text{foreground}}$, then an estimate of the foreground can be subtracted from the observed signal for a given source.

To provide an estimate of the foreground, we adopt the following procedure. Using the Gaussian fit parameters, we determine an annulus of width $1'$ with an inner radius of $2.57 \times \text{FWHM}$ ($1/100$ peak emission). This is sufficiently far from the source pixels, yet close enough that the signal measures the foreground adjacent to the source. We then determine the median value of the pixels within this annulus for each band of Stokes Q and U . Typically, about 100 pixels lie within the annulus. We subtract these foreground estimates from the corresponding FWHM pixels of the compact source. An example of a polarized source, the FWHM region and the foreground annulus region, is illustrated in figure 3.

The polarization angle, τ , is defined to be

$$\tau = \frac{1}{2} \tan^{-1} \frac{U}{Q} \quad (2)$$

within the range of 0° to 180° . Measured polarization angles are assumed to be the ‘wrapped’ result (ie. within the defining angle range) of some initial polarization angle, τ_o , plus a contribution from Faraday rotation such that

$$\tau' = \tau_o + \lambda^2 \text{RM}, \quad (3)$$

where τ' is the ‘unwrapped’ polarization angle. RMs are therefore calculated as the slope of the graph of unwrapped polarization angles versus the square of corresponding the wavelengths.

In previous studies, where the observation frequency bands were often several GHz apart, unwrapping the polarization angles and calculating the RM was carried out using an iterative approach, where integer multiples of π are added to the different bands until the residual on the corresponding fitted slope is minimized (ex. Simard-Normandin et al. 1981; Clegg et al. 1992). A significant advantage of the ST data is that the four sub-bands are so closely spaced we can calculate RMs directly and unambiguously using information from Stokes Q and U which would normally be lost when calculating polarization angles.

Previously determined RMs in the CGPS region range in magnitude from roughly 10 to 1000 rad m^{-2} . A RM of 1000 would correspond to a polarization angle difference between

the two central sub-bands of 49 degrees. Similarly, a polarization angle difference of 90° would correspond to a RM of 1840 rad m^{-2} , larger than what we expect based on previous measurements. As a result, we can use Stokes Q and U to directly unwrap the polarization angles in the following way. We consider a vector defined by Stokes Q (x axis) and Stokes U (y axis), and call it the ‘QU vector’. The phase differences between QU vectors in adjacent sub-bands will be twice the polarization angle differences (see equation 2), and since the expected polarization angle differences should be less than 90° , the phase differences between adjacent QU vectors should be less than 180° , making them uniquely determined in a four-quadrant plane. With the phase differences uniquely determined, the unwrapped polarization angles in each band are calculated by adding successively one-half of the phase difference between the QU vectors to the polarization angle of the chosen reference band A. Once unwrapped polarization angles are calculated, it is straightforward to calculate linear least-squares fit to the data, and therefore determine a RM for a given pixel (see equation 15 in the appendix).

Vallée (1980) discussed the importance of measuring RMs in the Faraday-thin, one-component regime for a given source. One technique to identify the Faraday-thin regime is to verify the linearity of the relationship between the polarization angle and λ^2 by testing the quality of the linear least-squares fit, using a basic ‘probability of fit’ test which compares the resulting best fit to the data (see, for example, Taylor 1997). If the average probability of fit across the S:N-thresholded FWHM pixels is less than 10%, we conclude that the measurements are not consistent with a linear relationship resulting from a Faraday-thin regime and we discard the source.

3.3. Step 3: RM Calculation per Source

To obtain a single value for the RM of sources that have survived critical analysis to this point, we calculate the ‘weighted average’ using the RMs calculated from the appropriate pixels of the source. The weighted average for the source (RM_w) is calculated as

$$\text{RM}_w = \frac{\sum_i (\text{RM}_i \times w_{\text{RM}i})}{\sum_i w_{\text{RM}i}} \quad (4)$$

where $w_{\text{RM}i}$ is the weight of each pixel (equation 18 in the appendix) and the sum is over the S:N thresholded FWHM pixels.

The final selection criterion we impose is the verification that the calculated RM is well behaved over the pixels on the source. In particular, we want to ensure that assigning a single RM value to the source is appropriate. For example, if there is more than one component, this will be manifested as different RMs within the FWHM region, or perhaps as a gradient

in RM across the source. A gradient across the source may also result from variations in the foreground which were not removed in the foreground subtraction method described in section 3.2. Whatever the cause, a single value of RM is not appropriate for the source, and we remove such sources from the RM catalogue.

For single value verification, we begin by assuming that any RM variations across the pixels within the FWHM region are due to errors produced by noise in the measurement and are therefore normally distributed. With this assumption, we apply the ‘Reduced Chi-Squared Test’. The reduced chi-squared, χ_r^2 , is

$$\chi_r^2 = \frac{1}{N-1} \sum_i \left(\frac{\text{RM}_w - \text{RM}_i}{\sigma_{\text{RM}i}} \right)^2 \quad (5)$$

where $\sigma_{\text{RM}i}$ is the uncertainty in RM for pixel i (see equation 17 in the appendix) and the number of degrees of freedom is equal to the number of pixels being averaged (N) minus 1, since there is one constraint (RM_w) calculated from RMs of the FWHM pixels. If the value of chi-squared is within the parameters of the test (we have chosen the 95% confidence level), then our assumption is most likely correct. In particular, we expect that a calculated chi-squared would only fall above the identified cut-off level 5% of the time (and thus be thrown out), assuming a Gaussian distribution of errors.

4. Results

Using this procedure, we have examined over 700 polarized sources in the CGPS. Of these, 380 sources satisfied the criteria described in §3. Figure 4 is a plot of the extragalactic RM sources in the CGPS region. This figure highlights the density of the CGPS sources, which is approximately 1 source per square degree.

Prior to this work, there were roughly 800 extragalactic sources with published RM across the entire sky. Of these, approximately 120 have lines-of-sight primarily through the Galactic plane ($|b| < 8^\circ$). The data presented here increases the number of extragalactic RM values by roughly 50% and the number of such sources with coordinates in the disk is more than quadrupled.

Table 1 is a list of the RMs of the CGPS sources. The columns of the table are as follows: column 1 and 2, the source position in Galactic longitude (l) and latitude (b); columns 3 and 4, the source position in right ascension (α) and declination (δ); column 5, the integrated flux density estimated from the two-dimensional Gaussian fit parameters of the source in the final release CGPS Stokes I images; column 6, the average value of the

fraction of linear polarization (m) across the S:N-thresholded FWHM pixels calculated from the interferometric data alone; column 7, the RM and error. The uncertainties in the values of the integrated flux densities are within $\pm 10\%$ (unless otherwise noted).

Many of the CGPS sources in table 1 have been previously identified in radio-source catalogs, but we could find previously determined RMs for only 5 of them. Eight other RM sources in the regions examined here had been previously identified, but did not pass our selection criteria. Table 2 compares the measurements from previous studies with those from the CGPS. The columns of table 2 are as follows: column 1 and 2, the source position in Galactic longitude (l) and latitude (b); column 3 and 4, previous RM measurements of the source; column 5, RM measurements from the CGPS; column 6, pass/fail indication for the CGPS measurement with respect to the procedure described in §3. As shown, source failure was often due to the χ^2 test, indicating a single value of RM could not be assigned to the source. In addition, most of the failed sources had insufficient polarization or the observation wavelengths of the ST were not within the Faraday-thin regime of the source. While the signs for all but one of the ‘failed’ sources are the same as the previously determined RMs, the difference in magnitudes range from 10% – 400%. Conversely, the difference between the ‘passed’ sources and previously measured RMs are all less than 30% (all but one are less than 20%). Of the sources that passed, small differences from previously measured RMs may be the result of differences in observation and calculation techniques. In addition, larger differences may be partially explained by time variations in the ISM along the line-of-sight to the source. The previously determined RMs are based on observations taken 10 – 20 years prior to the CGPS. Small perturbations in n_e and/or \mathbf{B} could account for some of the observed differences in RM. There may also be some contribution from time-variation effects from within the sources.

Figure 5 is a histogram of the CGPS RM distribution overlaid with the distribution of previously published EG RMs in the longitude range of the CGPS with $|b| > 20^\circ$. The high latitude sample provides an estimate of the intrinsic RM distribution of extragalactic sources, since the effect of the intervening ISM is expected to be small at these latitudes. The CGPS sample has a broad negative tail and the peak is shifted relative to the high latitude sources by approximately 1 bin (100 rad m^{-2}), indicating a general trend toward larger magnitude RMs for low latitude sources. The effect of the ISM in the Galactic disk is clearly present. The observed trends are consistent with the expected larger values of n_e for lines of sight at low latitudes, as well as the higher concentration of the magnetic field in the disk. Understanding the latitude dependence of RM is important for understanding the vertical structure of the Galactic magnetic field. The density and location of the CGPS sources will provide an excellent opportunity to study this latitude dependence (Brown et al. in preparation).

As well as the latitude dependence, the CGPS sources allow for the exploration of both the large and small-scale components of the magnetic field. For example, Brown & Taylor (2001) used these sources to show there is likely no reversal in the magnetic field direction beyond the solar circle, and that the distribution of the small scale field may be anisotropic. Future studies using these data and the additional data that will be available from the complete CGPS, will lead to significant advances in our knowledge of the Galactic magnetic field.

J.C.B. would like to thank E. Donovan for insightful discussions and assistance in accessing and visualizing the data effectively. The authors also thank the following individuals for polarization data processing: T. Bellchamber, C. Brunt, R. Kothes, M. Peracaula, C. Stewart, and B. Uyaniker. The DRAO Galactic Plane Survey is a Canadian project with international partners. The Dominion Radio Astrophysical Observatory is operated as a national facility by the National Research Council of Canada. The Survey is supported by a grant from the Natural Sciences and Engineering Research Council of Canada. This work was supported in part by the Alberta Ingenuity Fund Associateship program.

APPENDIX: Error analysis

In this section we provide the key elements of the error analysis used to derive the errors in the RMs listed in table 1.

Uncertainty in Stokes Q and U

When a CGPS mosaic is created, the individual fields are combined with specific “weights” applied to the pixels of the field. The weight at the center of a field, which has been normalized to one, is larger than at the edge of the field so that the weight map of a mosaic has an inverted ‘egg carton’ appearance, as illustrated in figure 6.

An estimate for the uncertainty in each pixel (i) of Stokes Q and U for each band (j) is

$$\delta Q_{ij}^2 = \delta U_{ij}^2 = \sigma_{\text{QU}i}^2 \quad (6)$$

where

$$\sigma_{\text{QU}i}^2 = \left(C_{\text{QU}} \sqrt{\frac{1}{w_{\text{QU}i}}} \right)^2 + (\alpha_c I_i)^2 . \quad (7)$$

Here, C_{QU} , the rms noise in the center of an individual field map, is the scaling factor for the weights, w_{QU} , and α_c is a fractional constant of the Stokes I . By adopting equations 6 and 7, we are assuming the uncertainty in Q_{ij} and U_{ij} is band-independent. C_{QU} is set equal to the noise-limited rms level (see §2). The term $\alpha_c I$ is included to account for uncertainty in the instrumental polarization correction procedure. The adopted value of $\alpha_c = 0.003$ is the maximum mean difference between the band-dependent and band-independent polarization correction factors (see appendix E of Brown 2002).

Signal to Noise for Linear Polarized Intensity

Linear polarized intensity is defined as

$$L = \sqrt{Q^2 + U^2}. \quad (8)$$

The signal-to-noise (S:N) for the linear polarized intensity for a given pixel i is defined as (Papoulis 1984):

$$\text{S:N}_{L_i} = \frac{L_i - (\text{noise bias})}{(\text{noise variability})} \quad (9)$$

Here, the noise variability is δL_i , while the noise bias is the expected ‘linear polarized intensity’ in the absence of signal, or:

$$\text{noise bias} = \frac{\sum_j \sqrt{\delta Q_{ij}^2 + \delta U_{ij}^2}}{4} = \sqrt{2}\sigma_{\text{QU}i} \quad (10)$$

Thus, the S:N relation is

$$\text{S:N}_{L_i} = \frac{L_{ci}}{(\sigma_{\text{QU}i}/2)}, \quad (11)$$

where

$$L_{ci} = L_i - \sqrt{2}\sigma_{\text{QU}i} \quad (12)$$

is the corrected linear polarized intensity.

Uncertainty in Polarization Angle

The polarization angle for a given pixel (i) in an given band (j) is calculated from Stokes Q and U using equation 2. The uncertainty in the angle is determined by the propagation of errors (assuming Q and U are independent to first order) and is given by

$$\delta\tau_{ij} = \sqrt{\left(\frac{\partial\tau_{ij}}{\partial Q_{ij}}\delta Q_{ij}\right)^2 + \left(\frac{\partial\tau_{ij}}{\partial U_{ij}}\delta U_{ij}\right)^2}. \quad (13)$$

Taking the appropriate derivatives, and recalling that $\sigma_{\text{QUI}} = \delta Q_{ij} = \delta U_{ij}$, the uncertainty becomes:

$$\delta\tau_{ij} = \frac{\sigma_{\text{QUI}}}{2(Q_{ij}^2 + U_{ij}^2)^{\frac{1}{2}}} = \frac{\sigma_{\text{QUI}}}{2 L_{ij}} \quad (14)$$

where L_{ij} is the linear polarized intensity in the specified band at the specified pixel.

Uncertainty in RM

The slope of the least-squares fit line for equation 3 (ie. the RM for a given pixel i) is determined from the relation (Press et al. 1997):

$$\text{RM}_i = \frac{\sum_j w_{ij} \sum_j w_{ij} \lambda_j^2 \tau_{ij} - \sum_j w_{ij} \lambda_j^2 \sum_j \tau_{ij}}{\Delta_i} \quad (15)$$

where

$$\Delta_i = \sum_j w_{ij} \sum_j w_{ij} (\lambda_j^2)^2 - \left(\sum_j w_{ij} \lambda_j^2 \right)^2, \quad (16)$$

λ_j is the wavelength of band j , and the weights, w_{ij} , are given by $w_{ij} = 1/\delta\tau_{ij}^2$. The resulting uncertainty in RM for the pixel i is

$$\sigma_{\text{RM}i} = \sqrt{\frac{\sum_j w_{ij}}{\Delta_i}}. \quad (17)$$

Using the uncertainty in the RM for each pixel to define the weights as

$$w_{\text{RM}i} = \frac{1}{\sigma_{\text{RM}i}^2}, \quad (18)$$

the uncertainty in the RM for the source is given as

$$\delta\text{RM}_w = \frac{1}{\sqrt{\sum_i w_{\text{RM}i}}}, \quad (19)$$

where the sum is over the S:N thresholded FWHM pixels.

REFERENCES

- Brown, J. C. 2002, Ph.D. Thesis, University of Calgary
 Brown, J. C. & Taylor, A. R. 2001, ApJ, 563, L31

- Broten, N. W., Macleod, J. M., & Vallée, J. P. 1988, *Ap&SS*, 141, 303
- Butenhoff, C. L. 1997, M.Sc. Thesis, University of Calgary
- Clegg, A. W., Cordes, J. M., Simonetti, J. H., & Kulkarni, S. R. 1992, *ApJ*, 386, 143
- Gaensler, B. M., Dickey, J. M., McClure-Griffiths, N. M., Green, A. J., Wieringa, M. H., & Haynes, R. F. 2001, *ApJ*, 549, 959
- Gray, A. D., Landecker, T. L., Dewdney, P. E., Taylor, A.R., Willis, A. G., & Normandeau, M. 1999, *ApJ*, 514, 221
- Han, J. L. & Qiao, G. J. 1994, *A&A*, 288, 759
- Landecker, T. L. et al. 2000, *A&AS*, 145, 509
- Oren, A. L. & Wolfe, A. M. 1995, *ApJ*, 445, 624
- Papoulis, A. 1984, *Probability, Random Variables, and Stochastic Processes* (New York, NY: McGraw-Hill, Inc.)
- Press, W. H., Teukolsky, S. A., Vetterling, W. T., & Flannery, B. P. 1997, *Numerical Recipes in C, The Art of Scientific Computing* (2d ed; New York, NY: Cambridge Univ. Press)
- Smegal, R. J., Landecker, T. L., Vaneldik, J. F., Routledge, D. & Dewdney, P. E. 1997, *Radio Sci.*, 32, 643
- Simard-Normandin, M., & Kronberg, P. P. 1980, *ApJ*, 242, 74
- Simard-Normandin, M., Kronberg, P. P., & Button, S. 1981, *ApJS*, 45, 97
- Taylor, A. R., Goss, W. M., Coleman, P. H., van Leeuwen, J. & Wallace, B. J. 1986, *ApJS*, 107, 239
- Taylor, J. R. 1997, *An Introduction to Error Analysis* (2d ed; Sausalito, CA: Univ. Sci. Books)
- Taylor, A. R. 1999, in *ASP Conf. Ser. 168, New Perspectives on the Interstellar Medium*, ed. Taylor, A. R., Landecker, T. L. & Joncas, G. (San Francisco: ASP), 3
- Taylor, A. R. et al. 2002, *AJ*, submitted
- Thompson, A. R., Moran, J. M., & Swenson, Jr., G. W. 2001, *Interferometry and Synthesis in Radio Astronomy* (2d ed.; New York, NY: John Wiley & Sons Inc.)

Vallée, J. P. 1980, *A&A*, 86, 251

Wieringa, M. H., de Bruyn, A. G., Jansen, D., Brouw, W. N., & Katgert, P. 1993, *A&A*, 268, 215

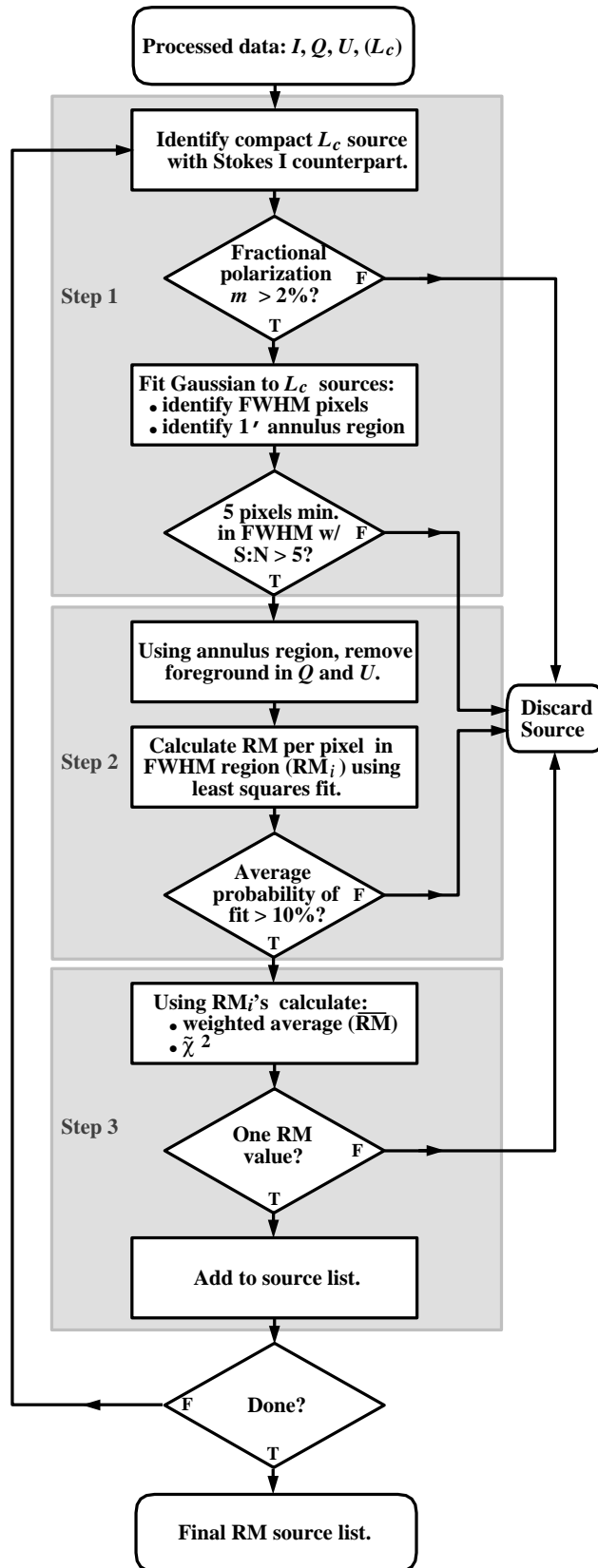


Fig. 1.— Flow chart of the RM calculation process.

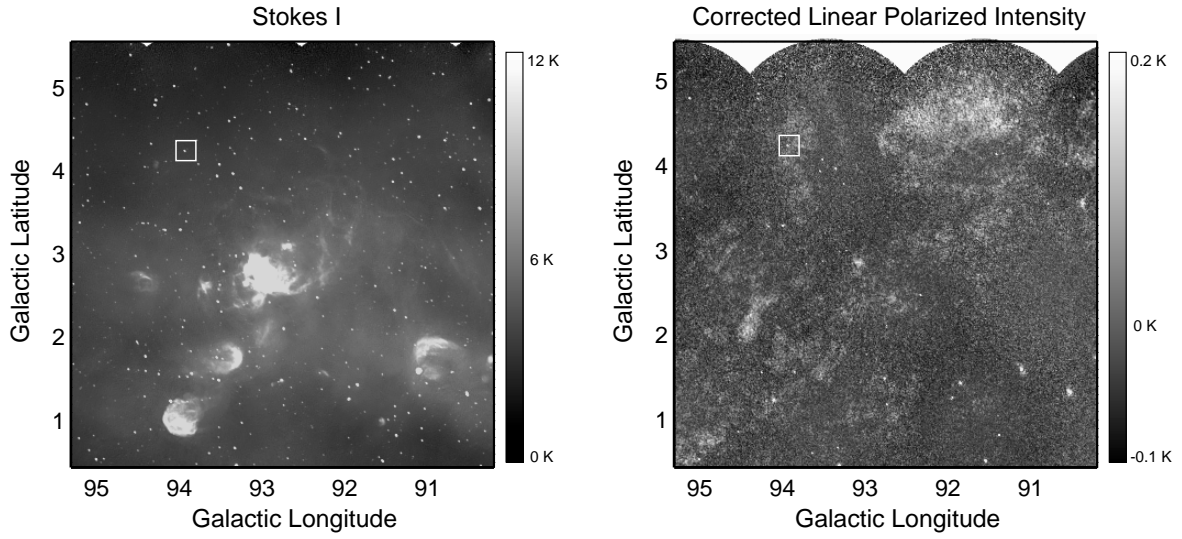


Fig. 2.— Canadian Galactic Plane Survey (CGPS) mosaic in total intensity (I , left panel), and corrected linear polarized intensity (L_c , right panel). The negative values in L_c result from the lack of zero-spacing data. The box highlights the source illustrated in figure 3.

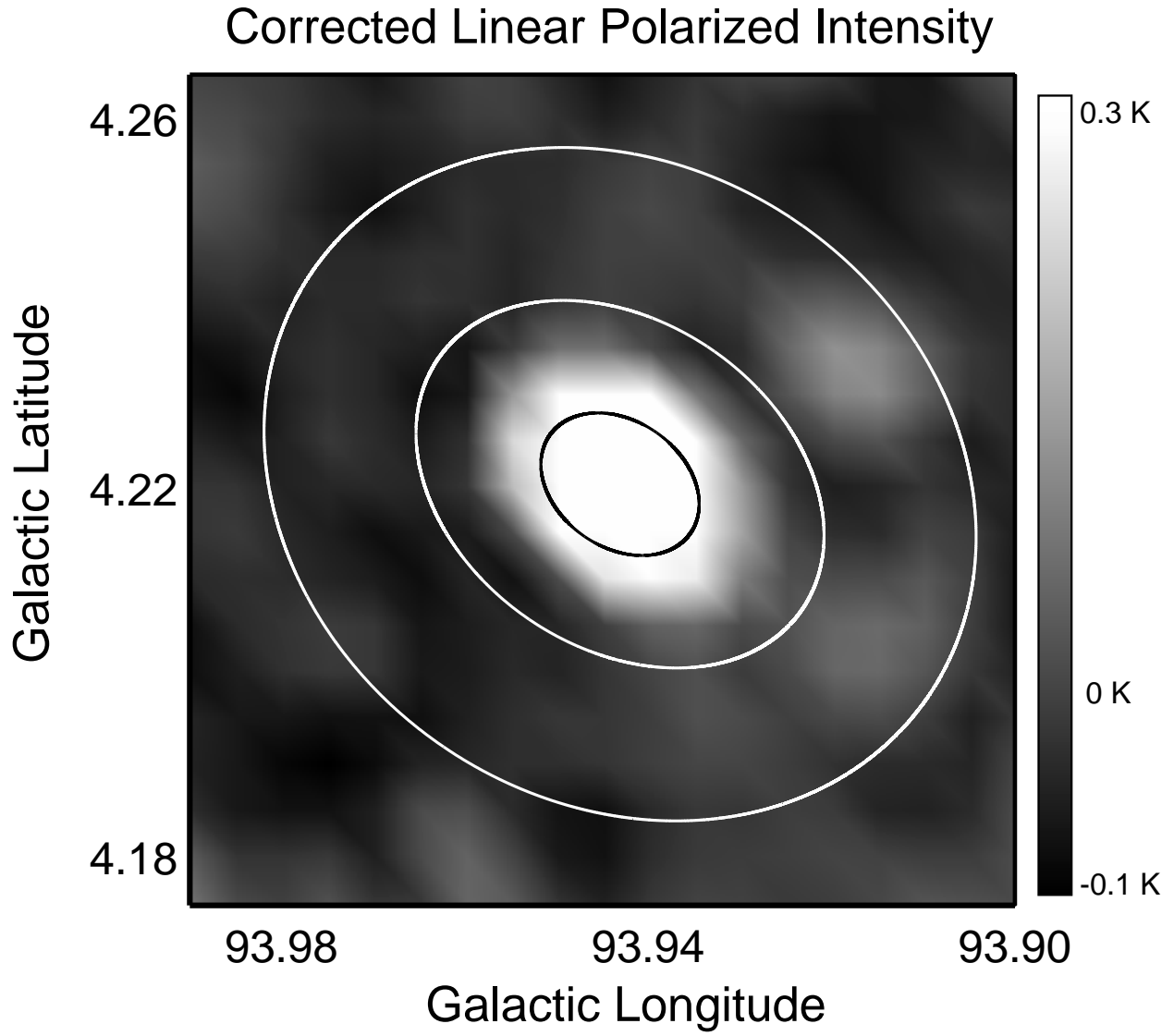


Fig. 3.— Polarized source highlighted in figure 2. The black contour indicates the FWHM level (0.45 K) while the white contours indicate foreground annulus boundaries.

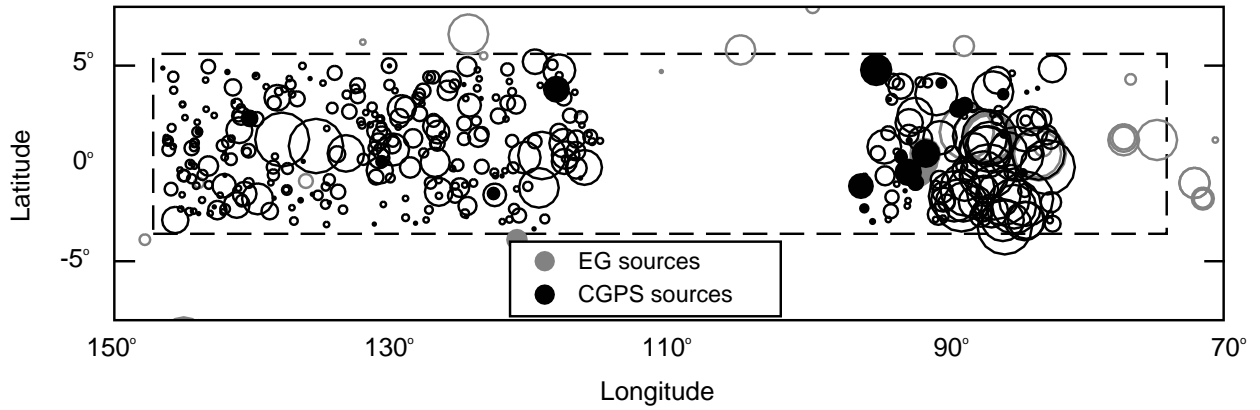


Fig. 4.— CGPS region (indicated by the dashed box) in rotation measure: dark symbols are CGPS sources, light symbols are previously studied sources. Source symbols are scaled to the magnitude of the RM, to a maximum of 700 rad m^{-2} (legend symbols are 100 rad m^{-2}). Filled circles are positive RM; open circles are negative RM. Data between $75^\circ < l < 82^\circ$ and $96^\circ < l < 115^\circ$ are not yet available.

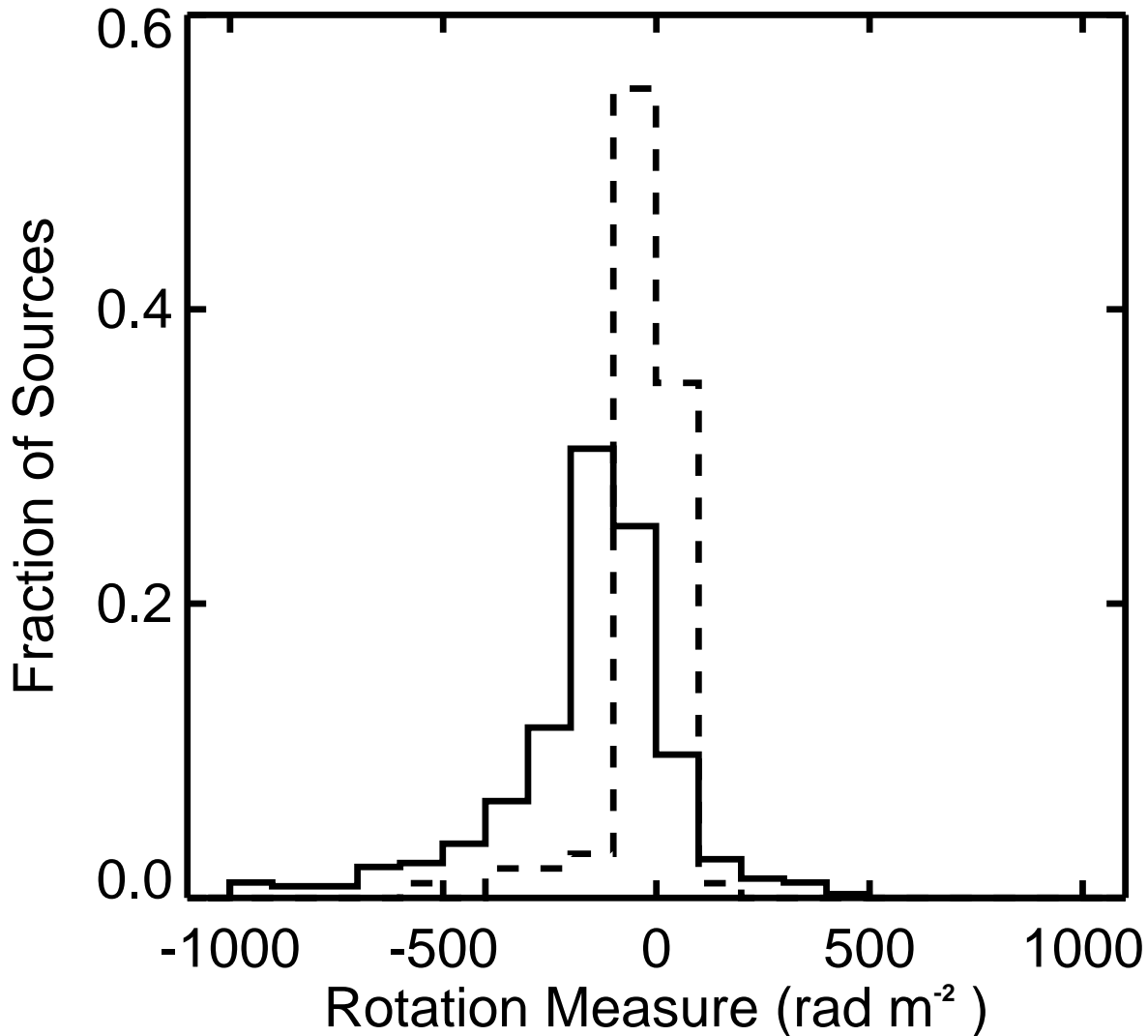


Fig. 5.— Histograms of the RMs of extragalactic sources. The solid histogram is the distribution for the 380 CGPS sources presented here with $-3.6^\circ < b < 5.6^\circ$; the dashed histogram is the distribution for previously published EG sources in the longitude range of the CGPS with $|b| > 20^\circ$ (100 sources). The bin size is 100 rad m^{-2} .

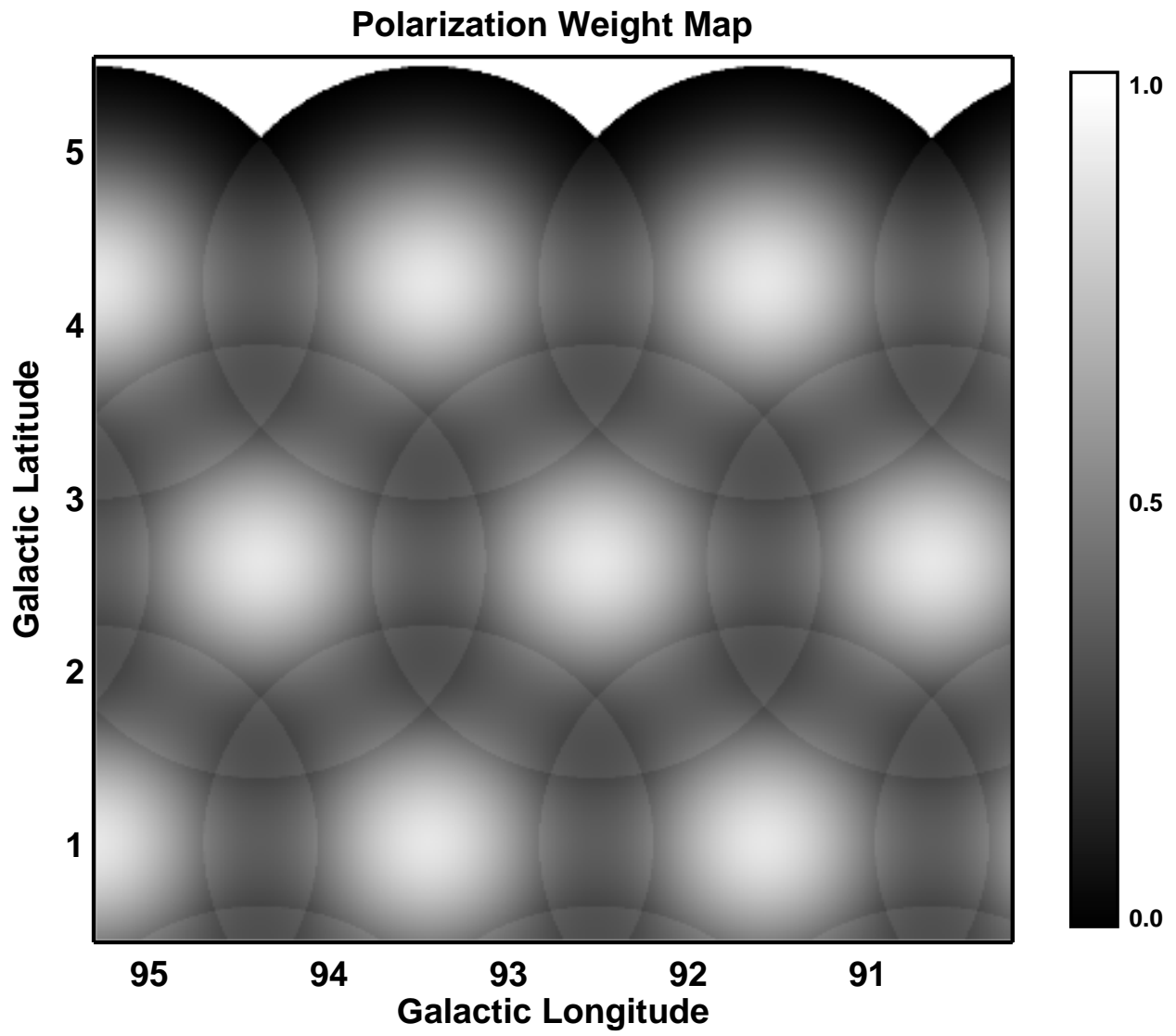


Fig. 6.— Polarization weight map for a mosaic in the CGPS.

Table 1. Rotation Measures of the CGPS

l ($^{\circ}$)	b ($^{\circ}$)	α (J2000)	δ (J2000)	I (mJy)	m (%)	RM (rad m $^{-2}$)
146.51	4.88	04 09 16.7	58 22 42	70	6.1	27 \pm 28
146.26	1.33	03 50 47.3	55 51 11	67	3.5	-58 \pm 28
146.13	1.16	03 49 21.9	55 47 44	83	3.7	-127 \pm 23
146.13	1.14	03 49 13.2	55 47 10	142	6.2	-78 \pm 11
146.08	0.71	03 47 06.1	55 28 50	38	9.0	-164 \pm 24
145.91	-1.32	03 37 43.1	53 57 59	129	4.1	-165 \pm 28
145.87	1.82	03 50 52.2	56 28 48	149	4.8	-103 \pm 21
145.76	0.87	03 45 57.8	55 48 10	84	3.9	-40 \pm 19
145.76	4.44	04 02 46.8	58 33 10	282	4.8	-132 \pm 8
145.73	3.75	03 59 09.5	58 03 08	147	2.5	-93 \pm 20
145.61	-2.90	03 29 54.4	52 51 19	320	2.9	-338 \pm 15
145.27	-0.34	03 38 07.6	55 08 17	71	4.8	-34 \pm 23
145.22	-2.33	03 29 52.9	53 32 39	2325	5.4	-8 \pm 7
145.12	-1.61	03 32 08.1	54 11 47	93	2.8	-49 \pm 31
145.09	3.04	03 52 01.4	57 55 03	813	15.3	-24 \pm 3
145.09	3.01	03 51 52.8	57 53 39	791	9.0	-39 \pm 5
145.02	-0.62	03 35 32.5	55 03 16	174	10.3	-150 \pm 6
144.96	-0.63	03 35 08.0	55 05 03	140	12.7	-146 \pm 5
144.91	2.35	03 47 46.2	57 29 19	42	8.0	-46 \pm 19
144.61	-2.47	03 25 58.6	53 46 06	55	6.2	-98 \pm 29
144.54	-0.05	03 35 09.6	55 48 05	231	8.5	-117 \pm 6
144.52	-0.01	03 35 12.6	55 50 44	64	3.6	46 \pm 33
144.43	-0.79	03 31 30.2	55 15 40	243	3.1	-120 \pm 16
144.43	0.79	03 38 01.4	56 32 16	83	2.4	-185 \pm 30
144.29	-2.45	03 24 14.1	53 58 08	136	3.3	-56 \pm 15
144.27	0.83	03 37 17.1	56 39 42	100	4.0	-101 \pm 20
144.23	-0.14	03 32 56.3	55 54 24	108	5.5	-67 \pm 25
144.23 ^a	1.05	03 37 57.6	56 52 22	148	7.8	-111 \pm 10
144.21 ^a	1.07	03 37 56.2	56 53 37	148	4.4	-102 \pm 16
144.10	-1.14	03 28 11.2	55 09 21	739	3.7	-86 \pm 10

Table 1—Continued

l ($^{\circ}$)	b ($^{\circ}$)	α (J2000)	δ (J2000)	I (mJy)	m (%)	RM (rad m $^{-2}$)
144.03	1.61	03 39 15.2	57 26 21	84	6.9	-127 \pm 12
144.03	2.11	03 41 29.4	57 50 23	306	2.3	-65 \pm 19
143.93	-2.57	03 21 43.2	54 03 39	95	5.1	56 \pm 20
143.91	1.64	03 38 40.1	57 32 05	94	2.1	114 \pm 36
143.68	-1.88	03 22 54.8	54 46 37	143	5.3	-79 \pm 10
143.65	-0.59	03 27 44.4	55 51 49	101	8.0	-131 \pm 11
143.43	4.27	03 47 59.6	59 54 51	227	4.4	-7 \pm 11
143.38	2.78	03 40 36.5	58 45 31	138	11.6	-39 \pm 6
143.23	4.95	03 50 13.2	60 34 14	37	11.1	-175 \pm 28
143.23	-0.13	03 27 03.7	56 28 58	152	3.3	-251 \pm 17
143.20	-1.10	03 23 02.2	55 41 28	108	11.5	-103 \pm 13
143.10	-2.56	03 17 00.4	54 30 55	110	3.2	-49 \pm 30
142.80	2.46	03 35 32.4	58 50 38	90	4.2	-24 \pm 15
142.80	-2.22	03 16 27.0	54 57 13	48	5.9	37 \pm 31
142.58	-2.39	03 14 32.6	54 55 42	19	12.8	-239 \pm 23
142.38	-1.63	03 16 09.5	55 41 05	72	10.2	-38 \pm 10
142.21	0.92	03 25 07.4	57 54 56	95	4.2	-148 \pm 14
142.16	-2.48	03 11 41.7	55 03 49	345	2.8	-73 \pm 15
142.09	-1.14	03 16 13.1	56 14 59	52	5.3	-302 \pm 34
142.05	0.32	03 21 39.6	57 30 05	211	9.4	-85 \pm 6
142.05	0.53	03 22 30.0	57 41 04	31	7.2	46 \pm 27
142.03	-0.61	03 17 52.7	56 43 54	267	2.3	28 \pm 28
142.02	-2.33	03 11 24.5	55 16 06	238	4.2	-124 \pm 10
141.86	4.68	03 39 56.4	61 11 40	58	6.5	84 \pm 22
141.80	1.10	03 23 18.1	58 17 45	83	3.3	-156 \pm 23
141.60	0.22	03 18 25.6	57 39 32	56	8.5	-152 \pm 18
141.57	1.27	03 22 30.5	58 33 59	215	2.9	-83 \pm 18
141.46	3.89	03 33 27.9	60 47 43	96	3.3	-210 \pm 21
141.43	3.17	03 29 54.5	60 13 22	80	4.5	5 \pm 20
141.19	-2.13	03 07 01.4	55 51 41	89	4.5	-330 \pm 18

Table 1—Continued

l ($^{\circ}$)	b ($^{\circ}$)	α (J2000)	δ (J2000)	I (mJy)	m (%)	RM (rad m $^{-2}$)
141.18	3.05	03 27 42.7	60 15 28	54	5.0	-134 \pm 22
141.05	-1.28	03 09 17.6	56 40 00	37	6.6	-14 \pm 24
141.05	2.41	03 24 01.9	59 47 43	124	2.3	-131 \pm 23
141.00	1.70	03 20 36.4	59 14 13	51	9.0	-334 \pm 17
140.88	2.83	03 24 43.1	60 14 32	191	10.5	-105 \pm 5
140.87	2.44	03 22 55.9	59 55 18	476	8.3	-231 \pm 5
140.82	-1.91	03 05 31.8	56 13 59	88	4.1	-148 \pm 20
140.62	-1.56	03 05 32.0	56 38 25	83	2.6	-307 \pm 32
140.46	0.59	03 12 31.4	58 34 39	75	7.1	-105 \pm 13
140.33	0.65	03 11 56.1	58 41 36	113	5.2	-175 \pm 11
140.33	-1.00	03 05 39.2	57 16 07	201	3.7	-127 \pm 13
140.26	2.31	03 18 15.7	60 08 29	63	3.5	230 \pm 37
139.85	4.53	03 25 27.6	62 13 51	31	7.0	36 \pm 22
139.80	4.48	03 24 48.4	62 12 56	84	5.0	-82 \pm 19
139.76	2.27	03 14 41.3	60 22 29	42	6.2	-182 \pm 24
139.68	-1.82	02 58 36.6	56 51 50	69	3.1	-398 \pm 34
139.06	3.93	03 16 58.3	62 09 01	125	3.9	-50 \pm 20
138.80	-2.44	02 50 50.8	56 42 24	26	11.2	-212 \pm 21
138.73 ^a	-0.99	02 55 09.7	58 02 14	82	4.4	-57 \pm 30
138.55	-0.19	02 56 49.4	58 49 33	56	3.9	-168 \pm 28
138.55	-0.59	02 55 20.3	58 28 31	26	7.6	-145 \pm 32
138.49	-1.78	02 50 55.4	57 26 16	129	2.0	43 \pm 29
138.49	3.11	03 09 13.5	61 44 31	132	6.6	-173 \pm 11
138.43	0.36	02 57 56.0	59 21 59	295	4.1	-80 \pm 11
138.26	3.36	03 08 37.7	62 04 41	91	2.7	-331 \pm 31
138.16	3.68	03 09 14.1	62 24 26	121	10.4	-100 \pm 7
137.91	1.23	02 57 29.9	60 22 43	33	3.9	-693 \pm 33
137.75	3.81	03 06 42.2	62 43 13	574	4.2	-80 \pm 9
137.62	-1.35	02 46 28.1	58 12 30	75	17.9	-81 \pm 6
137.58	-1.36	02 46 06.7	58 12 51	75	14.2	-124 \pm 8

Table 1—Continued

l ($^{\circ}$)	b ($^{\circ}$)	α (J2000)	δ (J2000)	I (mJy)	m (%)	RM (rad m $^{-2}$)
137.52	-0.26	02 49 25.8	59 13 39	52	4.9	-142 \pm 20
137.40	4.34	03 06 22.2	63 21 29	23	8.1	-53 \pm 33
137.30	4.04	03 04 15.8	63 08 29	115	4.9	-127 \pm 20
137.21	-2.27	02 40 44.3	57 32 47	81	2.9	-46 \pm 24
137.20	3.54	03 01 23.4	62 45 24	95	3.9	-84 \pm 26
137.07	-2.95	02 37 45.6	56 58 51	146	2.9	-99 \pm 24
136.83	3.31	02 57 34.6	62 43 26	48	6.3	-193 \pm 23
136.58	-1.89	02 37 35.7	58 08 46	116	2.5	88 \pm 19
136.45	4.99	03 01 45.9	64 22 51	273	10.0	-85 \pm 5
136.39	0.11	02 42 32.3	60 02 31	20	10.9	61 \pm 41
135.90	4.34	02 54 31.8	64 04 05	97	6.7	56 \pm 11
135.74	-1.58	02 32 33.2	58 45 21	118	3.8	58 \pm 30
135.47	0.89	02 38 18.1	61 08 01	195	5.1	-924 \pm 13
135.33	-1.63	02 29 30.6	58 51 40	59	7.9	-121 \pm 15
134.97	4.11	02 45 57.5	64 16 19	126	2.8	-60 \pm 20
134.80	-2.10	02 24 22.4	58 37 13	228	3.4	-115 \pm 13
134.77	-1.18	02 26 42.4	59 28 47	197	16.9	-105 \pm 4
134.72	-3.13	02 21 06.3	57 40 52	60	5.9	-61 \pm 36
134.70	1.79	02 35 20.1	62 15 52	71	4.1	-52 \pm 22
134.52	-0.84	02 25 48.7	59 53 52	67	4.1	-145 \pm 22
134.51	-2.01	02 22 33.4	58 48 13	470	2.8	5 \pm 14
134.30	2.84	02 35 43.8	63 22 50	414	2.1	-138 \pm 18
134.13	4.63	02 40 52.9	65 05 42	162	2.5	-181 \pm 20
133.95	0.48	02 25 15.8	61 19 29	93	6.1	-206 \pm 18
133.88	-1.45	02 19 24.1	59 32 22	79	2.8	-185 \pm 27
133.53	-2.37	02 14 30.2	58 47 15	50	5.8	-108 \pm 28
133.32	0.52	02 20 25.8	61 34 48	198	4.2	-470 \pm 11
133.26	3.52	02 29 19.6	64 24 40	57	6.7	-107 \pm 17
133.07	2.66	02 24 51.3	63 40 23	159	7.5	-186 \pm 8
132.64	3.82	02 24 56.0	64 54 36	95	4.5	-113 \pm 16

Table 1—Continued

l ($^{\circ}$)	b ($^{\circ}$)	α (J2000)	δ (J2000)	I (mJy)	m (%)	RM (rad m $^{-2}$)
132.49	3.99	02 24 08.8	65 07 42	50	4.9	-189 \pm 25
132.47	3.45	02 22 11.2	64 37 27	19	10.0	-185 \pm 24
132.24	2.15	02 16 18.3	63 28 41	52	4.2	-97 \pm 25
132.16	1.97	02 15 03.4	63 19 48	331	3.5	-92 \pm 12
132.07	0.21	02 09 38.1	61 41 16	1067	8.0	-145 \pm 5
131.88	2.61	02 14 34.7	64 01 21	115	3.9	-27 \pm 14
131.56	1.98	02 10 02.4	63 31 40	125	2.2	-59 \pm 23
131.43	2.89	02 11 24.3	64 25 47	28	8.1	-119 \pm 22
131.27	-3.11	01 56 13.6	58 42 49	72	4.2	17 \pm 27
131.23	2.51	02 08 35.9	64 07 37	58	6.8	-10 \pm 15
131.23	0.79	02 04 10.5	62 28 48	98	4.3	-168 \pm 17
131.15	-0.70	02 00 10.1	61 04 14	131	3.9	-192 \pm 14
131.07	1.67	02 04 59.9	63 22 28	53	8.5	-258 \pm 16
130.96	1.10	02 02 40.1	62 51 26	51	13.5	-223 \pm 25
130.93	0.28	02 00 33.4	62 04 26	45	7.8	-266 \pm 21
130.88	-0.36	01 58 44.2	61 28 09	52	4.7	-338 \pm 31
130.87	2.27	02 04 49.0	64 00 01	136	3.2	-68 \pm 32
130.85	2.27	02 04 36.7	64 00 44	265	4.0	-102 \pm 11
130.77	1.89	02 02 56.9	63 39 51	79	6.7	-128 \pm 13
130.77	0.62	01 59 56.8	62 26 26	228	4.0	-211 \pm 12
130.74	0.10	01 58 32.5	61 56 46	53	4.1	173 \pm 50
130.73	1.44	02 01 33.4	63 14 26	54	3.5	-233 \pm 36
130.63	-2.10	01 53 12.4	59 50 46	38	14.2	-5 \pm 13
130.21	5.00	02 06 11.5	66 48 36	72	7.8	-191 \pm 22
130.19	4.02	02 03 11.9	65 52 17	63	9.4	-132 \pm 11
130.18	4.99	02 05 52.3	66 48 32	90	6.0	13 \pm 20
130.12	-0.75	01 51 47.8	61 16 55	166	5.1	-115 \pm 10
129.99	0.95	01 54 05.8	62 57 39	14	17.9	-221 \pm 34
129.94	1.15	01 54 05.6	63 10 01	69	4.9	-149 \pm 25
129.93	0.71	01 53 07.6	62 44 27	100	6.1	-413 \pm 13

Table 1—Continued

l ($^{\circ}$)	b ($^{\circ}$)	α (J2000)	δ (J2000)	I (mJy)	m (%)	RM (rad m $^{-2}$)
129.79	3.72	01 58 40.9	65 41 36	107	3.2	-65 \pm 22
129.55	1.86	01 52 14.7	63 56 53	52	5.2	-64 \pm 21
129.47	2.32	01 52 27.9	64 24 37	45	4.2	-238 \pm 26
129.32	2.79	01 52 07.8	64 54 08	481	2.2	-358 \pm 15
129.02	-1.79	01 41 10.8	60 29 32	158	4.0	-56 \pm 12
129.02	-2.78	01 39 39.1	59 31 33	31	9.1	-88 \pm 27
129.02	2.88	01 49 34.5	65 03 47	83	4.3	-267 \pm 21
128.69	-0.21	01 40 58.1	62 06 43	56	9.3	-263 \pm 17
128.48	1.29	01 41 40.3	63 36 53	32	5.9	-238 \pm 34
128.41	3.46	01 45 05.7	65 45 17	160	6.4	9 \pm 10
128.30	-3.06	01 33 43.7	59 22 12	41	25.2	2 \pm 11
128.10	3.33	01 41 50.6	65 41 26	122	14.8	-154 \pm 5
128.03	3.55	01 41 38.4	65 55 08	350	4.6	-145 \pm 9
128.01	2.55	01 39 34.7	64 56 30	226	2.2	-191 \pm 18
127.85	3.06	01 38 58.7	65 28 21	85	4.4	-10 \pm 17
127.75	3.72	01 39 15.3	66 08 19	62	9.1	-188 \pm 15
127.72	0.54	01 33 49.6	63 01 02	100	7.0	-118 \pm 13
127.54	-2.89	01 27 58.8	59 39 17	80	5.4	-56 \pm 21
127.34	-2.38	01 26 58.4	60 11 33	169	3.4	-100 \pm 15
127.33	4.41	01 36 19.1	66 53 54	86	7.8	-152 \pm 8
127.32	4.39	01 36 14.0	66 52 47	215	5.5	-32 \pm 9
127.22	-1.00	01 27 34.2	61 34 33	288	3.3	-149 \pm 15
127.05	4.41	01 33 30.1	66 56 26	32	6.1	-160 \pm 25
127.01	2.21	01 29 46.1	64 46 24	202	3.3	-167 \pm 15
126.98	1.90	01 29 04.4	64 28 34	83	5.2	-282 \pm 18
126.89	0.06	01 26 00.1	62 39 40	47	4.7	-375 \pm 33
126.84	0.99	01 26 40.9	63 35 39	182	2.8	-132 \pm 17
126.74	1.03	01 25 47.2	63 38 35	66	4.5	-189 \pm 24
126.69	1.61	01 26 05.2	64 13 26	86	2.8	-294 \pm 32
126.65	-0.84	01 22 58.5	61 48 15	506	2.1	-89 \pm 19

Table 1—Continued

l ($^{\circ}$)	b ($^{\circ}$)	α (J2000)	δ (J2000)	I (mJy)	m (%)	RM (rad m $^{-2}$)
126.63	-1.46	01 22 10.9	61 11 28	142	4.3	-358 \pm 15
126.62	-1.66	01 21 54.5	60 59 55	99	3.2	-82 \pm 29
126.33	1.46	01 22 38.3	64 07 33	166	4.8	-90 \pm 14
126.01	3.74	01 22 10.0	66 25 24	233	2.7	-254 \pm 17
125.81	4.18	01 20 41.4	66 53 19	35	6.0	-274 \pm 35
125.65	-0.26	01 14 57.2	62 29 35	17	14.1	-22 \pm 24
125.54	-0.33	01 13 56.9	62 25 41	185	3.4	41 \pm 19
125.50	4.05	01 17 25.6	66 47 51	19	13.1	-122 \pm 21
125.46	-1.65	01 12 20.1	61 07 10	72	11.2	-184 \pm 10
125.44	-1.17	01 12 32.4	61 36 15	260	2.3	-90 \pm 19
125.28	-0.09	01 11 52.6	62 41 38	112	6.2	-151 \pm 27
125.12	-1.24	01 09 46.3	61 33 33	280	5.4	-241 \pm 9
124.82	4.04	01 10 35.6	66 50 12	179	2.4	29 \pm 19
124.82	1.26	01 08 39.3	64 03 50	51	6.0	-160 \pm 20
124.79	2.05	01 08 55.0	64 51 14	139	2.5	-184 \pm 25
124.76	-1.11	01 06 51.7	61 42 44	103	2.6	-49 \pm 28
124.75	-2.56	01 06 02.3	60 15 38	58	10.0	-107 \pm 14
124.69	3.32	01 08 44.3	66 07 59	92	2.5	-9 \pm 47
124.64	-2.72	01 05 05.1	60 06 24	94	4.2	63 \pm 23
124.59	4.95	01 08 53.9	67 45 56	94	7.2	-246 \pm 16
124.57	-2.18	01 04 45.0	60 39 17	61	3.7	-232 \pm 30
124.42	2.98	01 05 53.3	65 48 37	43	5.3	-293 \pm 19
124.13	-1.00	01 01 35.0	61 50 54	49	7.1	-97 \pm 16
123.94	2.18	01 00 58.2	65 01 42	45	4.7	-122 \pm 28
123.87	3.85	01 00 50.3	66 41 59	47	3.5	-86 \pm 35
123.85	4.79	01 01 02.6	67 38 23	33	11.8	-44 \pm 21
123.80	1.36	00 59 21.5	64 12 49	223	3.6	-256 \pm 13
123.72	4.33	00 59 31.9	67 11 22	95	5.8	-58 \pm 13
123.58	3.32	00 57 49.9	66 11 02	79	6.9	27 \pm 15
123.54	1.51	00 57 02.7	64 22 13	92	4.5	-181 \pm 16

Table 1—Continued

l ($^{\circ}$)	b ($^{\circ}$)	α (J2000)	δ (J2000)	I (mJy)	m (%)	RM (rad m $^{-2}$)
123.54	-0.17	00 56 41.1	62 42 03	150	3.5	-180 \pm 18
122.69	-1.54	00 49 24.5	61 19 51	92	3.5	178 \pm 29
122.63	-0.46	00 48 49.0	62 24 37	206	3.8	-102 \pm 12
122.60	-1.61	00 48 39.9	61 15 36	26	14.4	-291 \pm 22
122.56	-0.63	00 48 11.2	62 14 40	139	5.6	-63 \pm 9
122.51	3.37	00 47 14.5	66 14 18	282	5.6	-84 \pm 8
122.34	2.43	00 45 45.8	65 17 43	104	2.1	-194 \pm 30
122.08	-0.64	00 44 04.2	62 13 10	34	8.3	12 \pm 16
122.06	-2.98	00 44 26.6	59 53 06	286	3.4	-34 \pm 19
121.87	-0.38	00 42 11.2	62 28 40	108	4.5	-42 \pm 16
121.79	2.28	00 40 34.2	65 07 22	132	2.8	-50 \pm 24
121.69	4.80	00 38 24.0	67 38 43	385	3.7	-159 \pm 12
121.67	3.10	00 39 00.4	65 56 10	119	3.1	-189 \pm 28
121.55	4.19	00 37 14.4	67 01 25	105	4.6	-12 \pm 13
121.54	-2.87	00 40 18.6	59 58 18	40	19.1	-83 \pm 11
121.35	1.15	00 36 59.8	63 58 39	87	7.3	-158 \pm 10
121.35	3.66	00 35 35.2	66 28 59	33	8.7	-101 \pm 22
121.28	-0.22	00 37 03.4	62 36 20	794	3.6	-143 \pm 10
121.21	-2.33	00 37 24.3	60 29 41	2359	8.5	-133 \pm 4
121.06	3.01	00 33 06.4	65 48 54	38	9.1	-232 \pm 19
121.02	-1.31	00 35 23.3	61 30 26	379	4.4	-60 \pm 12
120.85	-2.67	00 34 42.4	60 08 21	62	6.2	-181 \pm 19
120.44	0.29	00 29 23.8	63 03 36	107	3.6	-407 \pm 21
120.22	-1.17	00 28 36.6	61 34 36	76	3.0	-118 \pm 26
119.77	-3.35	00 26 36.5	59 22 09	45	10.4	48 \pm 28
119.72	1.13	00 22 12.4	63 48 51	206	6.1	-176 \pm 7
119.70	5.20	00 17 06.2	67 51 21	188	4.1	-317 \pm 20
119.42	-1.25	00 22 00.2	61 25 15	176	4.6	-510 \pm 18
119.32	4.00	00 14 59.2	66 36 39	95	4.2	-47 \pm 17
119.20	0.41	00 18 24.7	63 02 14	378	4.6	-611 \pm 9

Table 1—Continued

l ($^{\circ}$)	b ($^{\circ}$)	α (J2000)	δ (J2000)	I (mJy)	m (%)	RM (rad m $^{-2}$)
119.00	-2.84	00 20 05.5	59 47 31	35	10.5	-115 \pm 26
118.46	3.50	00 07 19.2	65 59 17	54	7.3	-113 \pm 24
118.45	5.05	00 04 24.6	67 30 22	156	3.4	-134 \pm 40
118.16	3.80	00 03 53.6	66 13 31	215	5.1	349 \pm 9
117.98	1.59	00 05 56.4	64 01 05	107	2.4	-224 \pm 24
117.96	4.50	00 00 31.6	66 52 43	90	4.5	-88 \pm 16
117.96	4.76	00 00 00.1	67 08 00	48	7.1	-411 \pm 29
117.64	3.36	23 59 39.7	65 41 52	71	5.1	-200 \pm 21
117.64	1.04	00 03 48.2	63 25 15	159	3.1	-367 \pm 16
117.59	0.10	00 04 54.9	62 29 18	39	4.7	-323 \pm 33
117.54	0.24	00 04 14.1	62 36 40	44	4.9	-84 \pm 28
117.50	0.43	00 03 34.8	62 47 43	543	2.6	-355 \pm 14
117.18	2.45	23 57 12.1	64 42 33	146	2.5	-183 \pm 21
116.83	3.64	23 51 26.0	65 47 54	101	2.5	-10 \pm 33
116.75	0.63	23 56 50.3	62 50 40	134	5.7	-238 \pm 12
116.74	-0.24	23 58 16.2	61 59 25	54	8.6	-271 \pm 23
116.72	1.25	23 55 24.7	63 26 38	95	5.6	-222 \pm 17
116.42	-0.75	23 56 33.9	61 25 33	31	5.1	66 \pm 25
116.39	2.37	23 50 09.0	64 27 17	38	9.5	-159 \pm 17
116.32	1.97	23 50 26.0	64 03 03	64	2.7	-33 \pm 33
116.14	-0.21	23 53 13.3	61 53 46	126	3.2	-448 \pm 20
115.80	1.49	23 46 55.0	63 27 35	30	6.0	-57 \pm 31
115.72	1.37	23 46 29.4	63 19 25	53	5.1	-179 \pm 18
115.59	1.12	23 45 52.5	63 03 09	260	4.1	-90 \pm 11
115.01	1.16	23 40 54.3	62 56 12	169	13.8	-77 \pm 5
96.23	-1.16	21 45 07.6	51 46 57	175	3.7	334 \pm 16
96.05	-0.96	21 43 25.7	51 48 58	39	6.8	23 \pm 27
95.98	-2.30	21 48 36.8	50 44 59	87	5.1	135 \pm 20
95.96	-0.66	21 41 42.8	51 59 12	26	17.7	-2 \pm 16
95.92	-0.66	21 41 31.2	51 57 58	38	13.5	15 \pm 12

Table 1—Continued

l ($^{\circ}$)	b ($^{\circ}$)	α (J2000)	δ (J2000)	I (mJy)	m (%)	RM (rad m $^{-2}$)
95.39	-2.97	21 48 25.7	49 51 14	97	5.2	92 \pm 20
95.13	4.78	21 12 10.5	55 19 56	161	4.6	419 \pm 15
95.01	0.52	21 31 58.8	52 14 01	324	2.6	-186 \pm 15
94.54	0.85	21 28 16.2	52 09 02	94	2.7	-432 \pm 42
94.48	-0.63	21 34 30.7	51 01 32	97	9.1	-245 \pm 9
94.26	1.55	21 23 44.5	52 27 12	110	4.8	-178 \pm 21
94.25	-2.87	21 42 41.7	49 12 00	60	6.3	-15 \pm 35
94.18	3.27	21 15 13.8	53 36 20	167	3.0	23 \pm 25
94.07	-2.45	21 40 09.2	49 23 55	76	3.2	-182 \pm 38
94.00	3.28	21 14 22.1	53 29 11	195	6.6	-140 \pm 13
93.99	-1.72	21 36 46.5	49 53 16	433	5.2	-170 \pm 8
93.95	4.22	21 09 28.3	54 05 21	89	7.7	-187 \pm 13
93.65	-1.06	21 32 26.6	50 08 57	168	8.2	-35 \pm 8
93.64	0.60	21 25 13.4	51 20 44	72	4.2	-82 \pm 21
93.56	-0.34	21 28 55.8	50 36 39	132	12.5	5 \pm 8
93.53	4.06	21 08 20.9	53 40 21	257	2.2	-144 \pm 23
93.36	3.95	21 08 08.8	53 28 36	231	3.3	-323 \pm 15
93.34	0.32	21 25 03.1	50 56 04	1001	4.9	181 \pm 9
93.32	0.46	21 24 21.5	51 00 54	1532	2.0	-111 \pm 15
93.04	-1.40	21 31 09.5	49 29 01	88	5.0	69 \pm 22
92.88	-2.18	21 33 40.5	48 48 16	104	9.1	-52 \pm 11
92.83	-1.90	21 32 17.9	48 58 16	129	2.6	-23 \pm 35
92.82	-0.46	21 26 06.6	50 00 50	40	6.0	354 \pm 26
92.78	1.48	21 17 17.7	51 21 21	189	4.7	-251 \pm 15
92.75	2.09	21 14 22.9	51 45 29	166	2.6	-352 \pm 39
92.75	1.17	21 18 34.8	51 07 11	40	11.5	94 \pm 18
92.34	2.46	21 10 46.9	51 42 50	157	3.6	-453 \pm 17
92.32	-1.02	21 26 19.0	49 15 24	251	2.4	195 \pm 19
92.27	-0.98	21 25 56.9	49 15 15	154	3.9	216 \pm 11
91.95 ^b	1.25	21 14 42.1	50 36 16	273	2.6	-306 \pm 17

Table 1—Continued

l ($^{\circ}$)	b ($^{\circ}$)	α (J2000)	δ (J2000)	I (mJy)	m (%)	RM (rad m $^{-2}$)
91.95	4.16	21 00 51.3	52 33 49	38	7.0	-126 \pm 26
91.55	0.51	21 16 19.2	49 47 53	514	5.5	371 \pm 7
91.42	4.12	20 58 48.5	52 08 30	133	7.1	-117 \pm 9
90.85	-1.13	21 20 24.9	48 09 22	73	7.4	-125 \pm 15
90.85	-2.87	21 27 36.9	46 54 38	86	8.4	-61 \pm 21
90.80	3.54	20 59 02.4	51 17 14	113	4.4	-540 \pm 21
90.65	-2.60	21 25 41.7	46 57 46	48	6.5	-272 \pm 28
90.57	-0.83	21 17 58.6	48 09 52	69	2.8	-227 \pm 41
90.53	1.32	21 08 20.8	49 36 45	2106	6.1	-430 \pm 6
90.44	4.11	20 54 43.3	51 23 22	207	2.9	155 \pm 21
90.34	-1.48	21 19 45.2	47 32 27	19	17.5	-265 \pm 23
90.31	-2.80	21 25 04.1	46 35 10	43	7.3	-28 \pm 37
90.30	-1.85	21 21 09.5	47 15 18	40	6.9	-309 \pm 27
90.07	-2.01	21 20 50.9	46 58 33	15	17.1	-212 \pm 27
89.66	2.75	20 58 07.8	49 54 33	61	7.9	51 \pm 20
89.63	0.49	21 08 18.8	48 23 17	29	6.4	-197 \pm 37
89.51	-1.68	21 17 11.5	46 48 44	101	3.1	-651 \pm 23
89.27	2.77	20 56 29.3	49 37 48	171	6.8	215 \pm 9
89.18	2.82	20 55 52.2	49 35 50	116	3.3	239 \pm 22
88.98	-2.14	21 16 56.4	46 06 55	123	3.0	-679 \pm 34
88.97	-0.15	21 08 26.1	47 28 20	76	4.6	-142 \pm 36
88.85	-1.98	21 15 45.4	46 08 00	72	6.3	-503 \pm 20
88.78	2.42	20 56 08.2	49 01 47	19	11.9	-43 \pm 24
88.76	-1.11	21 11 44.6	46 39 40	25	7.0	-406 \pm 38
88.74	-0.31	21 08 15.1	47 11 42	92	3.6	-316 \pm 17
88.74	2.98	20 53 23.9	49 21 38	62	3.5	222 \pm 31
88.55	-1.31	21 11 45.2	46 22 42	84	4.6	-704 \pm 22
88.16	2.86	20 51 41.1	48 50 03	108	2.7	-115 \pm 29
88.08	0.80	21 00 46.7	47 26 18	69	5.1	-380 \pm 19
88.00	-1.99	21 12 24.7	45 30 30	67	3.0	-423 \pm 32

Table 1—Continued

l ($^{\circ}$)	b ($^{\circ}$)	α (J2000)	δ (J2000)	I (mJy)	m (%)	RM (rad m $^{-2}$)
87.64	1.40	20 56 23.2	47 30 18	382	4.9	-809 \pm 8
87.59	-2.69	21 13 41.7	44 43 46	169	4.6	-279 \pm 13
87.50	-2.46	21 12 26.8	44 48 56	155	2.2	-260 \pm 24
87.37	-0.61	21 04 11.2	45 58 44	61	3.5	-621 \pm 24
87.35	-1.34	21 07 11.5	45 28 15	14	11.2	-359 \pm 36
87.27	0.58	20 58 39.0	46 41 13	70	3.5	-662 \pm 27
87.08	0.75	20 57 10.6	46 39 13	78	2.7	-587 \pm 53
87.02	-0.41	21 01 56.9	45 51 00	470	3.4	-1413 \pm 10
86.98	1.35	20 54 07.5	46 57 56	621	4.4	-811 \pm 8
86.98	1.01	20 55 36.2	46 44 45	42	7.1	-563 \pm 25
86.82	-2.44	21 09 43.1	44 20 23	31	11.0	-424 \pm 30
86.73	3.67	20 42 29.5	48 13 50	43	8.2	-527 \pm 24
86.71	2.49	20 47 53.1	47 29 18	115	3.0	-65 \pm 21
86.63	-1.48	21 05 03.5	44 50 50	109	4.4	-909 \pm 18
86.40	2.23	20 47 55.8	47 05 02	482	3.3	-132 \pm 12
86.40	4.26	20 38 27.3	48 19 30	158	4.0	-346 \pm 14
86.31	2.73	20 45 19.8	47 18 58	41	6.7	-109 \pm 27
86.02	-1.77	21 03 57.8	44 12 11	90	4.6	-933 \pm 16
86.01	-2.90	21 08 34.2	43 25 47	64	3.7	-540 \pm 30
85.98 ^a	3.54	20 40 21.0	47 33 43	277	5.3	163 \pm 13
85.98 ^a	3.52	20 40 26.6	47 32 59	277	2.9	87 \pm 23
85.91	1.53	20 49 20.7	46 15 23	42	4.1	136 \pm 34
85.87	-3.27	21 09 32.6	43 04 34	73	9.0	-697 \pm 21
85.62	0.64	20 52 11.7	45 27 58	116	2.8	-482 \pm 22
85.38	-0.44	20 55 59.8	44 35 41	116	2.8	-181 \pm 24
85.34	4.61	20 32 58.7	47 41 23	119	3.3	-72 \pm 22
85.21	-2.19	21 02 43.4	43 18 43	93	3.5	-927 \pm 26
85.19	-2.21	21 02 46.3	43 17 03	143	4.5	-562 \pm 16
85.03	0.49	20 50 44.3	44 54 46	102	3.6	-759 \pm 22
84.55	-0.48	20 53 12.1	43 55 52	171	2.4	124 \pm 19

Table 1—Continued

l ($^{\circ}$)	b ($^{\circ}$)	α (J2000)	δ (J2000)	I (mJy)	m (%)	RM (rad m $^{-2}$)
84.45	-2.95	21 03 03.5	42 14 35	226	7.6	-496 \pm 8
84.43	-1.39	20 56 35.5	43 15 20	139	2.4	-167 \pm 26
84.36	2.19	20 40 48.3	45 27 09	113	3.7	-133 \pm 24
84.34	-1.81	20 58 01.1	42 54 50	577	4.0	-731 \pm 11
84.32	-2.91	21 02 27.1	42 10 08	76	6.8	-474 \pm 16
84.31	1.70	20 42 50.8	45 06 58	113	2.4	-550 \pm 32
84.28	3.65	20 33 52.7	46 16 13	126	4.1	69 \pm 17
83.95	2.18	20 39 27.1	45 07 07	118	2.2	-371 \pm 33
83.67	0.53	20 45 45.0	43 53 04	86	5.0	-173 \pm 20
83.50 ^c	3.85	20 30 18.1	45 45 36	382	2.6	27 \pm 19
83.45	0.51	20 45 05.9	43 41 49	477	2.7	-674 \pm 14
83.23	2.28	20 36 33.7	44 36 37	83	4.8	-258 \pm 18
82.80	1.46	20 38 45.3	43 46 20	33	9.5	-243 \pm 32
82.78	-0.20	20 45 49.7	42 44 26	151	4.1	-880 \pm 27
82.62	-2.91	20 56 30.6	40 53 09	47	7.3	-79 \pm 22
82.60	-2.58	20 55 05.2	41 05 14	109	2.9	-60 \pm 22
82.56	1.20	20 39 03.1	43 25 22	74	3.5	-228 \pm 28
82.54	-1.99	20 52 29.5	41 25 26	114	3.8	-263 \pm 16
82.44	4.84	20 22 10.1	45 28 10	168	2.3	-349 \pm 20
82.42	-3.09	20 56 32.8	40 37 27	120	7.0	-205 \pm 13

^aTwo separate components in L (one or both passed) and two unresolved components in I . I value represents the combined integrated flux density.

^bTwo components in L (only one passed), but only one identifiable component in I . I value represents the integrated flux density of the whole source.

^cOne component in L and two unresolved components in I . I value represents the combined integrated flux density.

Table 2. RM source comparison in the CGPS

l ($^{\circ}$)	b ($^{\circ}$)	RM (rad m $^{-2}$)			Pass/ Fail †
		Clegg et al. (1992)	Brotten et al. (1988)	CGPS	
91.55	0.51	410 \pm 4		372 \pm 7	P
90.53	1.32		-359 \pm 1	-430 \pm 6	P
87.64	1.40	-869* \pm 7		-809 \pm 8	P
86.98	1.35	-630* \pm 19		-811 \pm 8	P
83.45	0.51	-683* \pm 7		-674 \pm 14	P
143.9	-1.06		-128 \pm 2	-27 \pm 2	F: a, c, d
136.2	-0.90		-179 \pm 2	-164 \pm 6	F : d
120.56	1.20		409 \pm 2	-597 \pm 22	F: a, c, d
116.52	2.56		17 \pm 8	162 \pm 15	F: a, d
91.95	-0.53	322* \pm 4		243 \pm 22	F: a, c, d
91.71	0.08	355* \pm 3	347 \pm 3	172 \pm 5	F: d
88.59	1.63	-708* \pm 19		-846 \pm 39	F: a, b, c, d
83.10	0.81	-220 \pm 48		-884 \pm 22	F: c

† Failure codes: a. Fractional polarisation $<$ 2% (polarisation questionable); b. FWHM $<$ 5 pixels (insufficient size); c. Probability of fit $<$ 10% (not Faraday thin); d. χ^2 test failure (no single RM value).

*Source has multiple published components; weight-average RM value is given.